Electrochimica Acta 283 (2018) 949–958

Contents lists available at ScienceDirect

Electrochimica Acta

journal homepage: www.elsevier.com/locate/electacta

The first-principles study of $CoSb_2O_4$ and its electrochemical properties for supercapacitors

Amirthalingam Shanmugavani [a], Murugan Lalitha [b], Rajeesh Kumar Narayanan Kutty [a], Leonid Vasylechko [c], Yun Sung Lee [d], Senthilkumar Lakshmipathi [b], Ramakrishnan Kalai Selvan [a, *]

[a] Energy Storage and Conversion Devices Laboratory, Department of Physics, Bharathiar University, Coimbatore, 641046, India
[b] Atomistic Simulation Laboratory, Department of Physics, Bharathiar University, Coimbatore, 641 046, India
[c] Semiconductor Electronics Department, Lviv Polytechnic National University, 12 Bandera Street, Lviv, 79013, Ukraine
[d] Faculty of Applied Chemical Engineering, Chonnam National University, Gwangju, 500-757, South Korea

ARTICLE INFO

Article history:
Received 6 March 2018
Received in revised form
27 June 2018
Accepted 29 June 2018
Available online 30 June 2018

Keywords:
First principle study
Cobalt antimonite
Hydrothermal synthesis
A hybrid capacitor

ABSTRACT

By varying Co:Sb molar ratio, crystalline $CoSb_2O_4$ was synthesized through surfactant free hydrothermal method. The tetragonal crystal structure and phase composition of cobalt antimonate were obtained through XRD Rietveld refinement method. $CoSb_2O_4$ exhibits a direct band gap of 2.89 eV was computed using First-principle density functional theory (DFT) calculations. Here, the Fermi energy level is upshifted to conduction band region, representing the n-type behaviour of the $CoSb_2O_4$ unit cell. The oxidation state of +2 and + 3 of Co was identified through X-ray photoelectron spectroscopy analysis (XPS). Formation of submicron size, rod shape particles was confirmed by Transmission electron microscopic (TEM) images. Cyclic voltammogram exhibits a specific capacitance of 598 F g^{-1} at 2 mV s^{-1} in 1 M KOH. More importantly, Galvanostatic charge-discharge analysis (GCD) delivered the specific capacitance of 382 F g^{-1} at 1 mA cm^{-2}. For practical application, an asymmetric supercapacitor is constructed using $Ni_3(Fe(CN)_6)_2(H_2O)$ as a positive electrode and synthesized one-dimensional $CoSb_2O_4$ as a negative electrode, which offered a maximum specific capacitance of 279 Fg^{-1} at 1 mV s^{-1}. Cycling stability of the fabricated device demonstrated the retention of almost 100% and hence depicts its promising nature as an efficient electrode for supercapacitor application.

1. Introduction

Renewable and non-renewable energy sources are the two primary types of energy resources, where former one is abundant and cost-effective. Further, renewable energy sources have low carbon emissions and are considered as a green and environmentally friendly. However, the primary obstacles in these sources are its seasonal variation and variable energy output. In the case of non-renewable energy sources, the enormous exploitation has led to severe environmental changes due to the release of toxic gases into the air, which is the primary cause of the global warming. All these factors have instigated the researchers to explore the new possibilities of potential energy sources. Over the past few decades, supercapacitors are considered as a promising energy storage device, since it has high power density, long cycle life and fast charge-discharge ability [1].

Based on the underlying energy storage mechanisms, supercapacitors are classified into electric double layer capacitor (EDLC) and pseudocapacitors. In the EDLC type capacitors the charges stored through electrostatic interaction between the electrode/electrolyte interface utilizing the carbon-based materials including carbon nanotubes, activated carbon, graphene [2,3]. On the other hand, the pseudocapacitors involve redox reactions employing materials like transition metal oxides (NiO, Fe_3O_4, Co_3O_4, MnO_2, Mn_3O_4) [4–8], hydroxides ($Co(OH)_2$, $Ni(OH)_2$ [9]) and polymers (polyaniline, polypyrrole, polythiophene, and so on) [10]. However, the binary metal oxides are better-qualified candidates than the pure metal oxides due to their improved redox properties. Furthermore, they have demonstrated the higher capacitance, rate capability and better cycling stability. Hence, it is essential to explore a new type of binary metal oxide materials for the future

* Corresponding author.
E-mail address: selvankram@buc.edu.in (R. Kalai Selvan).

https://doi.org/10.1016/j.electacta.2018.06.193
0013-4686/

applications [11].

In this regard, the present investigation reports the supercapacitive performance of Pb_3O_4 type $CoSb_2O_4$ in aqueous electrolytes. In $CoSb_2O_4$ structure, antimony is present in +3 oxidation state and can be synthesized only under controlled conditions. It comes from the family of MSb_2O_4 with M = Mn, Fe, Ni, Zn [12]. Due to the unclear magnetic transition, no particular crystallographic and magnetic properties have been reported. Some of the cobalt-antimony based compounds have found in the literature such as $CoSb_3$ [13], $CoFe_3Sb_{12}$ [14] and $CoSb_2O_6$ [15] were used for various applications. Laune et al. has synthesized $CoSb_2O_4$ by a ground mixture of CoO and Sb_2O_3 at 700°C for 6 h and investigated the magnetic susceptibility measurements [16]. Further, Jibin et al. have studied the possibility of using $CoSb_2O_4$ as a negative electrode for Li-ion batteries and obtained the reversible capacity of 412 mA hg^{-1} [17]. However, no report is available for supercapacitor application.

Hence an attempt was taken to synthesize $CoSb_2O_4$ through hydrothermal synthesis by varying the mole ratios of Co and Sb precursors. The synthesized $CoSb_2O_4$ shows the direct band gap of 2.89 eV at the Γ point of the reciprocal space in the high-symmetry *k*-point region. Besides, the Fermi energy level is upshifted to conduction band region, indicating the n-type behaviour of the $CoSb_2O_4$ unit cell. Presence of +2 and + 3 oxidation states of Co 2p and +3 of Sb 3d peak favours the redox reaction. Further, rod-like morphology is revealed by FESEM and TEM. Importantly, the capacitance is found to be 598 F g^{-1} at 2 mV s^{-1} in 1 M KOH through cyclic voltammetry analysis. With this knowledge, an asymmetric supercapacitor is fabricated with $Ni_3(Fe(CN)_6)_2(H_2O)$ electrodes. This device offered the specific capacitance of 30 F g^{-1} at 1 mA cm^{-2} and achieved cycling stability of 100% over 1000 cycles. Hence this kind of new fabricated hybrid supercapacitors ($CoSb_2O_4$‖ $Ni_3(Fe(CN)_6)_2(H_2O)$) finds a better place in the forthcoming days.

2. Experimental section

2.1. Synthesis of $CoSb_2O_4$ by hydrothermal method

The analytical grade chemicals were purchased from MERCK INDIA Ltd and used for the synthesis. For the typical synthesis of $CoSb_2O_4$, the required amount of $Co(CH_3COO)_2.4H_2O$ and $SbCl_3$ were dissolved in double distilled water and conc. HCl, respectively. Subsequently, the dissolved individual precursor solutions were mixed under stirring, and the pH was changed to 10 by using 3.5 ml of ammonia solution. Afterwards, the mixed precursors were taken in Teflon lined stainless steel autoclave and placed in a muffle furnace for 24 h at 200 °C. After cooled down to room temperature, the collected precipitate was centrifuged with double distilled water and finally with ethanol to remove the organic impurities. Then the obtained pinkish grey product was dried at 100 °C for 12 h in an air oven. For each experiment, the mole ratio of Co: Sb was varied from 0.5 (CB1), 0.7 (CB2), 0.9 (CB3) and 1 (CB4) to achieve $CoSb_2O_4$ for subsequent reactions.

2.2. Material characterization

The structure and crystallinity of the prepared particles were investigated by performing XRD analysis using BRUKER-Germany, D8 Advanced model with 2.2 kW Cu anode as a source over the 2θ range of 10–80°. The elemental composition was identified using XPS analysis and is performed through Multilab 2000 (VG, UK), Ultra axis instrument. Further, the functional groups were determined from Fourier Transform Infrared analysis (FTIR) of Bruker Tensor 27 spectrophotometer and the sampling was done with KBr. The shape and size of the particles were envisaged through F E I Quanta FEG 200 - Field emission Scanning Electron Microscope (FESEM) and Transmission electron microscope (TEM) images of HRTEM (JEOL-JEM 2100). Significant electrochemical analysis such as Cyclic voltammogram (CV), galvanostatic charge-discharge analysis (GCD) and Electrochemical Impedance analysis (EIS) was carried out in electrochemical workstation BIOLOGIC SP 150 (France). EIS analysis was performed in the open circuit potential with an a.c. perturbation potential of 10 mV.

2.3. Electrode preparation and electrochemical measurements

For the electrochemical measurements, the electrodes were prepared by making a slurry using 70% of the synthesized $CoSb_2O_4$ as an active material, 20% of carbon black and 10% of PVdF with 0.3 ml of NMP. After that, the slurry was coated on the graphite sheet having an area of 1 cm^2 (1 × 1 cm), which is pretreated with ultrasonication using distilled water and dried. After coating, the wet electrodes were allowed to get dried at 100 °C in a vacuum oven for overnight. Finally, these were used as working electrodes for capacitive measurements. The electrochemical performances of the $CoSb_2O_4$ are investigated using three electrode cell configurations. It consists of working electrodes (active material coated electrodes), a counter electrode (Graphite sheet) and a reference electrode (Hg/HgO), respectively. Similarly for the full cell configuration, prepared $CoSb_2O_4$ as negative electrode and $Ni_3(Fe(CN)_6)_2(H_2O)$ coated electrodes as positive electrodes. For positive electrode preparation, the above-said procedure is followed. Then these electrodes were sealed by the poly tetra fluoro ethylene tapes (PTFE) to circumvent the leakage of electrolyte.

2.4. Computational details

The electronic structure calculation of the $CoSb_2O_4$ unit cell is performed based on the first-principles density functional theory (DFT) calculations using Vienna Ab-initio Simulation Package (VASP) [18]. The interactions between the electrons and the ions are described by the Projected Augmented Wave (PAW) method. The exchange-correlation potential is expressed using the Generalized Gradient Approximation (GGA) [19] proposed by Perdew, Burke & Ernzerhof (PBE) functional. The first Brillouin zone is sampled using Monkhorst-Pack grid of 6 × 4 × 2 k-point mesh for electronic structure calculations, and the kinetic energy cut-off of 500 eV is used for the expansion of the plane-wave basis set. The CIF file was obtained from the experimental data, and hence the single-point calculations are directly performed on the $CoSb_2O_4$ unit cell, and its lattice constants are listed in Table 1 (a = 8.486 Å, b = 8.486 Å and c = 5.941 Å). The effect of on-site Coulomb interactions due to the localization of 3d electron in Cobalt would result in self-interaction errors in DFT calculations, and hence the Dudarev [20] Hubbard model (DFT+U) approach has been employed in the computation. The U parameters are chosen as U = 5.4, 5.6, 5.8 and 6.0 eV, which would result in improvement of the band gap.

3. Results and discussion

3.1. Crystal structure and density of states

The crystal structure of $CoSb_2O_4$ consists of 28 atoms per unit cell (obtained as CIF file from experimental data) is shown in Figs. S1a and b. The electronic properties such as band structure, the partial density of states (pDOS) plot and the spin-polarized DOS plot of the $CoSb_2O_4$ unit cell are provided in Fig. 1a, b and 1c respectively. The band structure of $CoSb_2O_4$ exhibits a direct band gap of 2.89 eV at the Γ point of the reciprocal space in the high-

Table 1
Crystal structural parameters of $CoSb_2O_4$.

Cell parameter	GGA	GGA+U				Experimental Values
		U = 5.4	U = 5.6	U = 5.8	U = 6.0	
a (Å)	8.486	8.486	8.486	8.486	8.486	8.486
b (Å)	8.486	8.486	8.486	8.486	8.486	8.486
c (Å)	5.941	5.941	5.941	5.941	5.941	5.941
Volume/cell ($Å^3$)	427.87	427.87	427.87	427.87	427.87	427.87
Total energy (in eV)	−169.99	−165.35	−165.22	−165.08	−164.95	–
Bond length (Å)						
Co–O	1.976, 2.092	2.047, 2.244	2.047, 2.244	2.047, 2.244	2.047, 2.244	–
Sb–O	2.025, 2.056	2.018, 1.966	2.018, 1.966	2.018, 1.966	2.018, 1.966	–
Eg (Band gap) in eV	2.89	2.78	2.78	2.78	2.78	–
Local Magnetic moment of Co (μ_B)	2.562	2.780	2.787	2.794	2.801	2.7
	$s+p = 0.01$	$s+p = 0.03$	$s+p = 0.03$	$s+p = 0.03$	$s+p = 0.03$	
	7	1	1	1	1	
	$d = 2.545$	$d = 2.749$	$d = 2.756$	$d = 2.763$	$d = 2.770$	

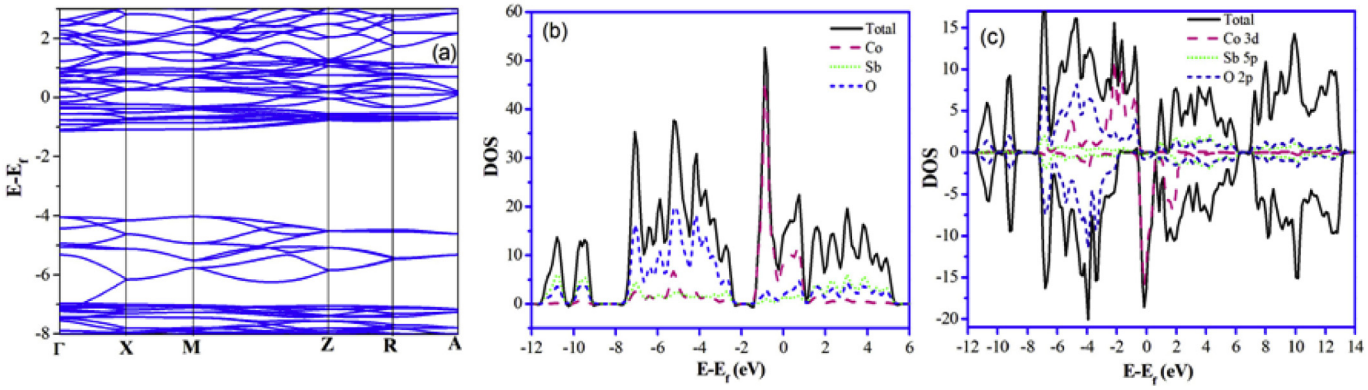

Fig. 1. (a) Band Structure of $CoSb_2O_4$ unit cell (Bandgap = 2.89 eV) (b) The PDOS plot (c) Spin-polarized DOS plot.

symmetry *k*-point region. Besides, the Fermi energy level is upshifted to conduction band region [18–22], representing the n-type behaviour of the $CoSb_2O_4$ unit cell. From the pDOS plot, Co in $CoSb_2O_4$ produces prominent states in both the Fermi energy region and near the valence and conduction band region. Besides Co, the other main contribution to DOS is from the oxygen atom in the high-lying valence band regions. From the spin-polarized DOS plot, a small band gap is evident from the spin-up region, whereas in the spin-down Co states are prominent in the Fermi energy region. Spin-up Co states and spin-down Co states play an essential role in the valence band edge and the conduction band edge region respectively. The valence band region is dominated by O *2p* orbitals, whereas the high-lying regions of the conduction band region are equally contributed by Sb *5p* and O *2p* orbitals. The spin-polarized density of states plot in Fig. S2a–d shows the effect of on-site Coulomb interactions on $CoSb_2O_4$ for the different U values. The lattice parameters, the volume of the cell, the band gap of the unit cell and the local magnetic moment of Co atom for varying U values are listed in Table 1. The lattice parameter and the cell volume of the unit cell remain unaltered, whereas the significant change in band gap is observed. The band gap value of 2.78 eV for the different U values are consistent with the band gap of 2.89 eV obtained through the band structure calculations (GGA). Further, the band gap for the different U values and the density of states plot appears to be consistent. The local magnetic moment of Co atom is 2.562 μ_B, which is linearly increasing up to ~2.8 μ_B due to the Coulomb interactions (c.f. Fig. S3), consistent with the experimental value of 2.7 μ_B. However, from Table 1, the $s + p$ moment of Co remains consistent for the increase in U value, whereas 3d moment increases, which subsequently leads to the increase in the total magnetic moment. Furthermore, the total energy of the system increases linearly on varying the U parameter, which is attributed to the reduction in Sb–O and elongation of Co–O bond length (c.f. Table 1).

3.2. Structural analysis

The XRD pattern of synthesized $CoSb_2O_4$ with different Co: Sb mole ratio is shown in Fig. 2a-d. The secondary phases of Sb_2O_3 are obtained while using a stoichiometric mole ratio of Co: Sb precursor (0.5). Whereas on increasing the mole ratio from 0.5 to 0.9, the intensity of Sb_2O_3 phase gets reduced. However, the decomposition of $CoSb_2O_4$ occurs at a ratio 1, and again the secondary phases are started to appear. Hence it is confirmed that the excess of Co and Sb ratio (0.9) may be an optimum concentration for the formation of $CoSb_2O_4$.The percentage of Sb_2O_3 phase is estimated using the XRD intensity calculations (eqn. (1) in supporting information). The obtained percentage of Sb_2O_3 phase is 27 and 15% for CB1 and CB2 samples, respectively. On the other hand, no trace of Sb_2O_3 phase is observed for CB3 sample. The similar kind of calculation has been reported for $CuCo_2O_4$ [23], $CuFe_2O_4$ [24] and $NiCo_2O_4$ [25] compounds. The obtained diffraction planes well matched with the standard pattern of tetragonal $CoSb_2O_4$ (JCPDS No. 89-1613). However, the sample (CB3) with nominal composition "$CoSb_2O_4$" shows a two-phase composition. Besides the primary Pb_3O_4-type tetragonal $CoSb_2O_4$ phase, it contains some amount of the parasitic phase, which could be identified as cobalt hydroxy-chloride $Co_2(OH)_3Cl$ (PDF card 73-2134).

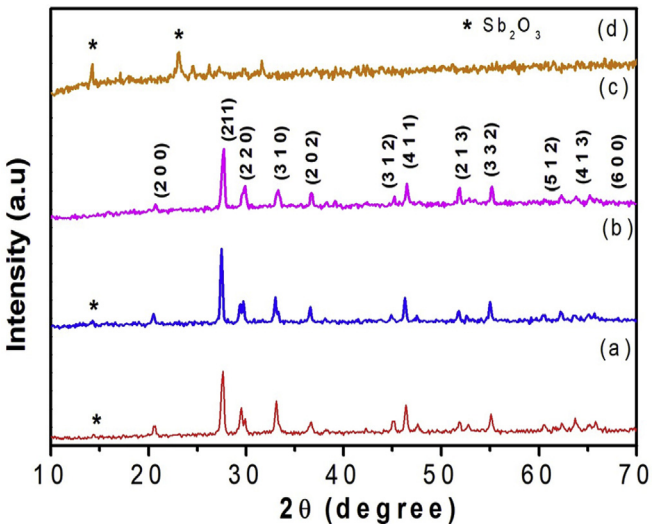

Fig. 2. XRD pattern of synthesized $CoSb_2O_4$ by varying the Co:Sb mole ratio (a) CB1 (0.5), (b) CB2 (0.7), (c) CB3 (0.9), (d) CB4 (1).

The two-phase full-profile Rietveld refinement performed by using WinCSD software [26] confirmed the phase composition (Fig. 3). According to the results of quantitative full-profile Rietveld refinement, the sample consists of 90.5 wt. % of $CoSb_2O_4$ and 9.5 wt. % of $Co_2(OH)_3Cl$ (Fig. 3). As starting models in the refinement procedure, the atomic positions in $CoSb_2O_4$ [16] and $Co_2(OH)_3Cl$ [27] were used. Refined structural parameters of the $CoSb_2O_4$ phase and final residuals are presented in Table 2. Refined structural parameters and cell dimensions of $CoSb_2O_4$ structure in the samples analysed are in good agreement with the literature data (Table 3). Based on the refined structural parameters on $CoSb_2O_4$ structure presented in Table 3, the interatomic distances were calculated (Table 4). The Pb_3O_4-type of the MSb_2O_4 structure commonly described as chains of edge-linked MO_6 distorted octahedra running along the [001]-direction [16,29–31]. The $^1{}_\infty[MO_4]$-chains are connected via pyramidal SbO_3 units, creating the tunnel structure, as in the case of our previously reported $NiSb_2O_4$ [32].

XPS analysis is carried out to identify the elemental composition for the synthesized $CoSb_2O_4$ (CB3) and the respective spectrum is shown in Fig. 4a. The survey spectrum exhibits the presence of Co, Sb and O element. For further insight, the deconvoluted spectrum of Co 2p (Fig. 4b) shows two peaks at binding energies of 780.59 eV and 796.26 eV corresponding to Co $2p_{3/2}$ and Co $2p_{1/2}$, respectively [33], which reveals the fact that Co is present in both the +2 and + 3 valence states. Additionally, two satellites peaks observed at higher binding energies of 787.02 eV and 802.26 eV along with the Co 2p peaks. Further, the peak at binding energies of 530.34 eV and 539.56 eV attributes to Sb $3d_{5/2}$ and Sb $3d_{3/2}$ (Fig. 4c) [34]. Moreover, the presence of O 1s is revealed along with the Sb $3d_{5/2}$ at 529.68 eV (Fig. 4d) through the deconvoluted two more peaks at 530.79 eV and 528.38 eV [35]. This is due to the presence of lattice oxygen species and oxygen from the surface functional groups, respectively [36].

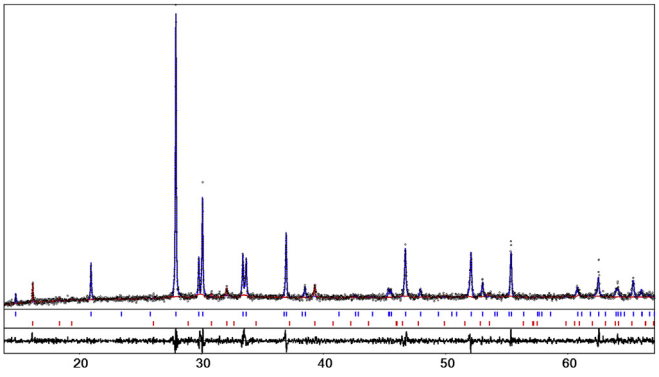

Fig. 3. Graphical results of two-phase Rietveld refinement showing coexistence of $CoSb_2O_4$ (blue) and $Co_2(OH)_3Cl$ (red) phases in the "$CoSb_2O_4$" sample. Experimental XRD pattern is shown in comparison with the calculated patterns. The difference between measured and calculated profiles is shown as a curve below the diagrams. Short vertical bars indicate the positions of diffraction maxima of $CoSb_2O_4$ and $Co_2(OH)_3Cl$ (upper and lower rows, respectively). (For interpretation of the references to colour in this figure legend, the reader is referred to the Web version of this article.)

The FT-IR spectral analysis was performed to identify the presence of functional groups in the synthesized $CoSb_2O_4$ (CB3) and is shown in Fig. S4. It is seen that Sb–O stretching vibration is observed in the range (380-800 cm^{-1}). The band observed at 493 cm^{-1} represents the Sb–O stretching vibration [37]. Also, the band observed at 632 cm^{-1} ascribes the strong interaction of Sb with residual oxygen-containing groups in the Sb–O bond [38].Further the peak at 1025 cm^{-1} and 1109 cm^{-1} attributes to the Sb–OH band. The peak formed at 1421 cm^{-1} infers the Sb–OH stretching. Further, the peak observed at 1636 $cm^{-1}$and the band around 3500–3900 cm^{-1} attributed to the H–O–H and O–H bending and stretching vibrations of surface hydroxyl groups of adsorbed water molecules of the material. The peak observed at 2110, and 2336 cm^{-1} represents the second overtone of Sb–OH band [38].

3.3. Morphological analysis

The shape and size of the synthesized $CoSb_2O_4$ (CB3) can be evidenced through FESEM images and is shown in Fig. S5a. It is seen that there is a formation of 1 D rod shape morphology in the micrometre size range. Fig. S5b shows the magnified images which illustrate the formation of rods in the material. Moreover, these rods are like a rectangle in shape within the micrometre range. The particle size distribution is presented by plotting the histogram and is given in supporting information Fig. S5c&d. Fig. S5c and Fig. S5d show the average length and width of the particles in the micrometre size range of 1.5 μm to 2 μm (Fig. (S5c)) and 1.0 μm to 1.5 μm (Fig. (S5d)), respectively. Further, the recorded TEM images (Fig. 5a and b) shown that the material is composed of rectangular bars and exhibits 0.5–1 μm in length and about 0.5 μm in width. Further, Fig. 5c shows the single rod-like structure with 560 nm in length and 107 nm width. Fig. 5d–f shows the SAED pattern of the particles with the appearance of bright spots. These confirm that the single crystalline nature of the synthesized materials. Also, the d-spacing value is measured to be 3.0 nm from HRTEM images which is shown in Fig. 5e.

3.4. Electrochemical analysis of $CoSb_2O_4$ electrode (3 electrode system)

3.4.1. Cyclic voltammetry analysis

Electrochemical performance of the prepared electrode is investigated by performing cyclic voltammetry analysis by using Hg/HgO as a reference electrode. Fig. 6a shows the CV curves of the prepared CB3 electrode at various scan rates such as 1 mV s^{-1} to 50 mV s^{-1} in an aqueous 1 M KOH electrolyte. The nature of the CV curves indicates the presence of redox reaction in the prepared $CoSb_2O_4$ electrode and confirms that the charges are stored through the redox reaction. Further, it shows that on increasing the scan rate, the nature of the CV curves remains constant and shows the redox peaks. This indicates the better electrochemical rate

Table 2
Crystallographic data for $CoSb_2O_4$ (space group $P4_2/mbc$, $Z = 4$).

Lattice parameters, residuals	Atoms, sites	x/a	y/b	z/c	$B_{iso/eq}$, Å^2
$a = 8.4862(4)$ Å	Co, 4d	0	1/2	1/4	0.9(4)
$c = 5.9415(3)$ Å	Sb, 8h	0.1771(9)	0.1615(9)	0	0.46(13)
$R_I = 0.035$	O1, 8g	0.688(3)	x-1/2	1/4	0.9(10)
$R_{WP} = 0.114$	O1, 8h	0.086(5)	0.643(5)	0	0.9(11)

Table 3
Refined values of the lattice parameters of $CoSb_2O_4$ in comparison with the literature data.

a, Å	c, Å	V, Å^3	Refs.
8.4862(4)	5.9415(3)	427.84	This work
8.49340(9)	5.92387(8)	427.34	[29]
8.519(3)	5.932(2)	430.51	[31]
8.494(4)	5.922(2)	427.26	[28]

Table 4
Selected bond lengths (Å) with estimated standard deviations in parenthesis in the $CoSb_2O_4$ structure.

Co–O2 × 4	2.05(3)
Co–O1 × 2	2.25(3)
Sb–O2	2.01(4)
Sb–O1 × 2	1.96(2)
Sb–O2	2.78(4)

capability of the prepared $CoSb_2O_4$ electrode material. Further to know the electrochemical stability of the electrode, cyclic voltammogram is performed at 50 mV s^{-1} for 500 cycles and are given in Fig. S6. It can be seen that the current area covered by the voltammogram remains same for all the 500 cycles. It indicates the better electrochemical stability and its suitability for the supercapacitor application. From the cyclic voltammogram, the specific capacitance of CB3 electrode is calculated [39,40], and it shows the higher specific capacitance of 598 F g^{-1} at 2 mV s^{-1}. Comparatively, the obtained capacitance is much higher than the reported Co based compounds like $CoFe_2O_4$ nanoflakes (366 F g^{-1} at 5 mV s^{-1}), $CoFe_2O_4$ (123 F g^{-1} at 1 mV s^{-1}) and $CoMoO_4$ (394.5 at 1 mV s^{-1}) [41–43]. Further, the calculated specific capacitance at various scan rates is plotted and is shown in Fig. 6b. It confirms that by increasing the scan rate, the decrease in specific capacitance is observed for all the scan rates. This is due to the well-known

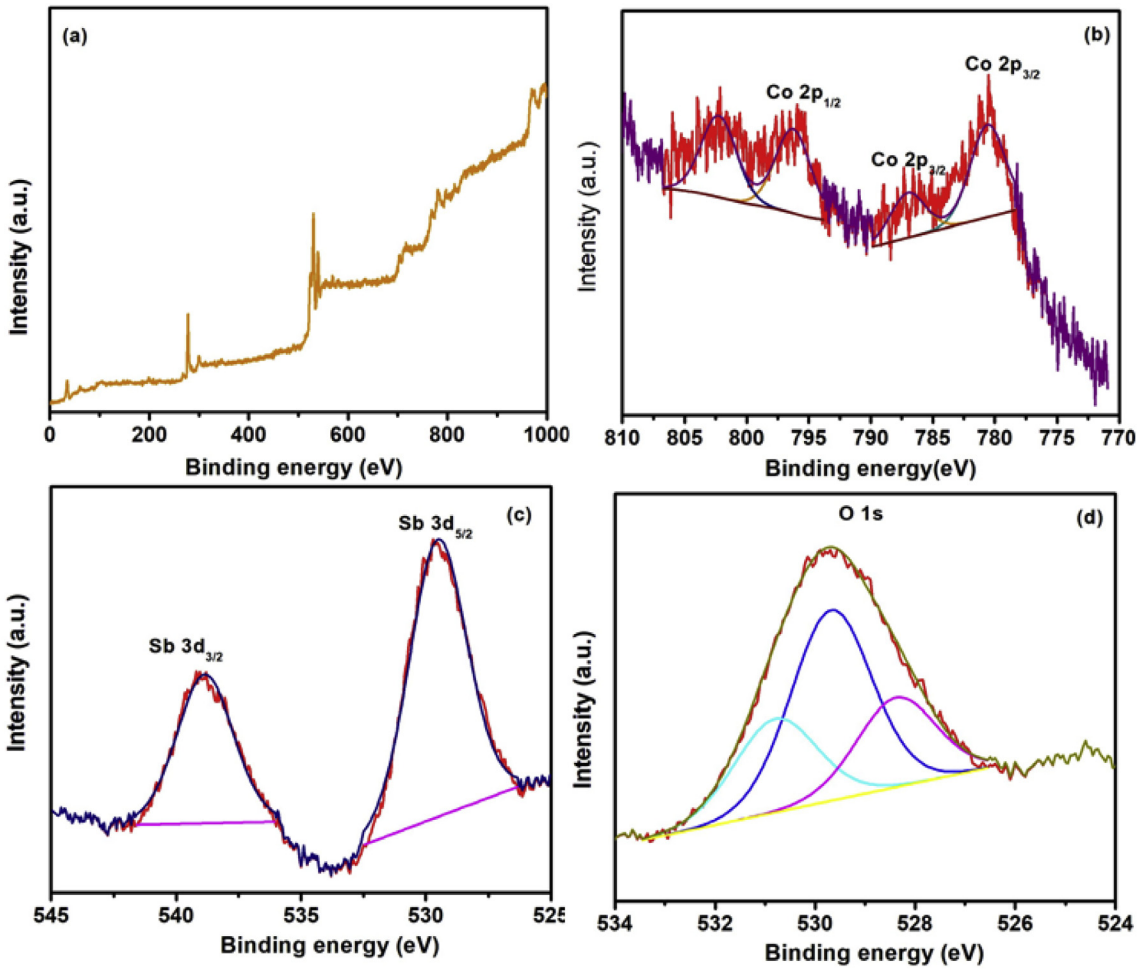

Fig. 4. XPS spectra of $CoSb_2O_4$ (a) survey, (b) Co 2p, (c) Sb 3d and (d) O 1s.

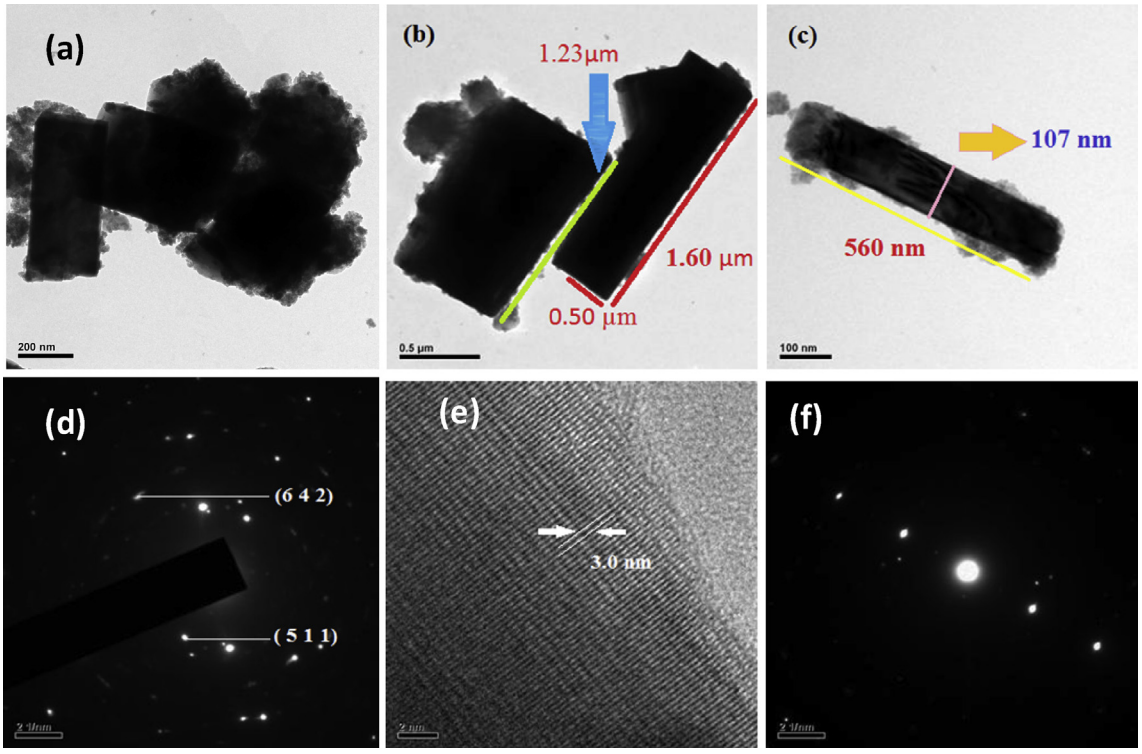

Fig. 5. (a, b & c) TEM image of CB3 at different magnifications, (d & f) SAED pattern and (e) HRTEM image.

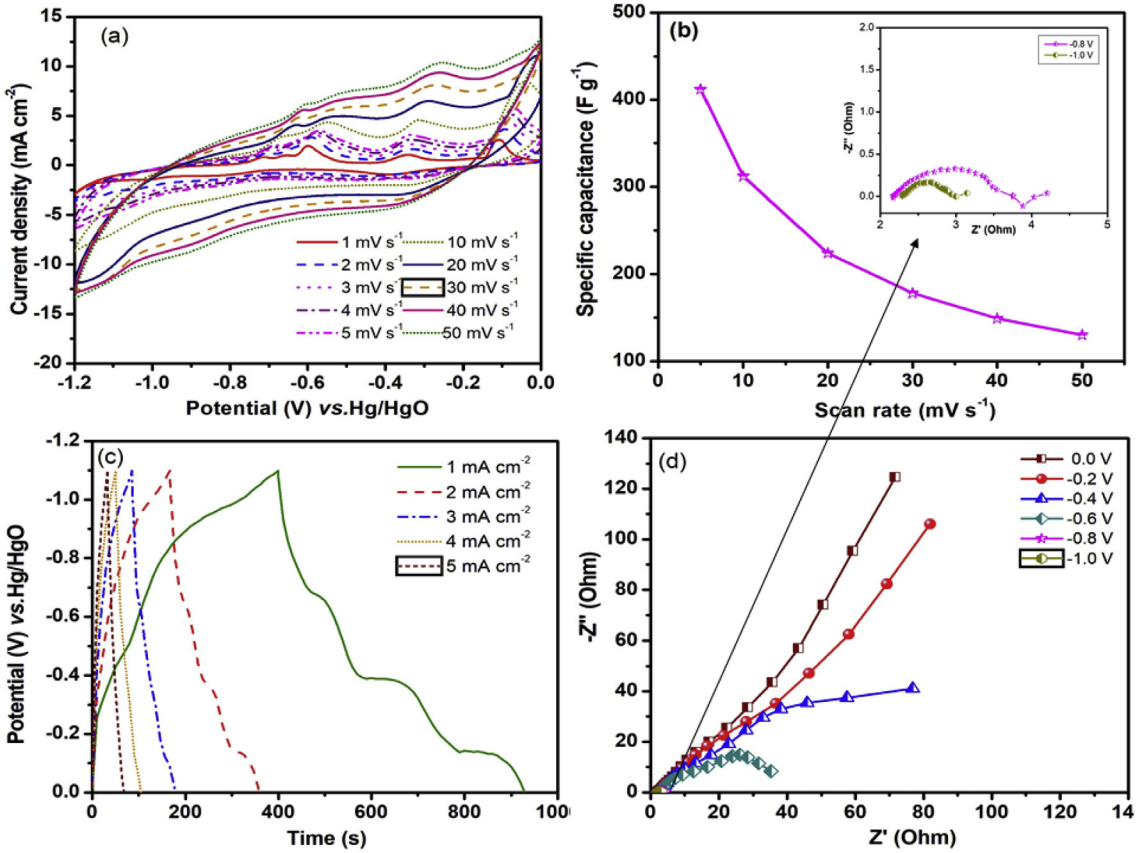

Fig. 6. CV curves of prepared (a) CB3 electrode at various scan rates in 1 M KOH (b) specific capacitance vs scan rate plot (inset shows the EIS spectra performed at bias potential −0.8 V and −1.0 V) (c) GCD curves at various current densities (d) impedance plot of CB3 electrodes at various bias potential.

electrochemical fact that, acquiring more time at low scan rate for an electrode, efficiently undergoes the electrochemical redox reaction at active sites. In case of applying high scan rate, a redox reaction occurs rapidly and hence some active sites could not be utilised and hence results in lower capacitance. Subsequently, the electrochemical surface areas (ECSA) is calculated from the linear charging region of CV curves at various scan rates (10, 20, 30, 40 and 50 mV s^{-1}) at a specific potential of −0.8 V for $CoSb_2O_4$ [44–46]. The non-faradaic current i_{DL} is determined by the charge accumulation in the linear charging region. The i_{DL} versus ν curves of the electrode measured at −0.8 V is given by equation (1)

$$i_{DL} = C_{DL}.\upsilon \quad (1)$$

here, C_{DL} is the double layer region specific capacitance and ν is the scan rate. The ECSA is calculated by using the following equation (2)

$$\mathrm{ECSA} = \frac{C_{DL}}{C_S} \quad (2)$$

C_s is the specific capacitance in alkaline electrolyte. The value of C_s is reported as 0.040 mF cm^{-2} in KOH electrolyte [44]. Using the above relations, the calculated ECSA for $CoSb_2O_4$ is 1.205 cm^2, which is comparable with the supercapacitor electrodes of graphene (0.068 cm^2), flower like copper doped Graphene Nanosheet (0.102 cm^2) [47] and Cobalt phosphide (1.535 cm^2) [48].

3.4.2. Charge-discharge analysis

The galvanostatic charge-discharge (GCD) analysis was performed for the prepared CB3 electrode at various current densities which are shown in Fig. 6c. The nature of the GCD curves is asymmetric; this substantiates that the pseudocapacitive mechanism is predominant in this electrode. It is a well known that, at low current density, the electrode exhibits its fundamental electrochemical redox reactions. In the present case, at a low current density of 1 mA cm^{-2}, three different plateau regions are observed during charging in the potential sweep from −1.2 V to 0.0 V (because it is performed in the negative potential window). To clearly understand the electrochemical activity and identify the exact peak potential, the dQ/dV curve is drawn and given in supporting information (Fig. S7). It can be seen that three well-distinguished peaks (−0.67, −0.38 and −0.14 V vs Hg/HgO) are observed corresponding to each plateau regions. It is the typical battery like behaviour and due to the redox reactions of Sb ions [49–51] and the alloying mechanism [17], since Sb has multiple oxidation states. Various authors have reported the similar kind of observations for Sb_2O_3 based anodes in non-aqueous Na-ion batteries [52–56]. However, the exact redox mechanism is yet to understand in future works. The specific capacitance of CB3 is calculated at various current densities and obtained the specific capacitance of 327 F g^{-1} at 1 mA cm^{-2}. This is much higher than the reported $Co_{3-x}Mn_xO_4$ hierarchical architectures (173 F g^{-1} at 0.15 A g^{-1}) [57]. Further CB3 electrode shows better performance than the cobalt-doped manganese nanostructures (415 F g^{-1} at 0.15 A g^{-1}), flower-like $CoMn_2O_4$ (188 F g^{-1} at 1 A g^{-1}), $CoMoO_4$ nanorods (89.5 F g^{-1} at 1 mA cm^{-2}) and plate-like $CoMoO_4$ nanorods (151 F g^{-1} at 1 mA cm^{-2}) [58–61]. These values infer the superior performance of prepared $CoSb_2O_4$ nanoparticles.

3.4.3. Electrochemical Impedance Spectroscopy (EIS) analysis

EIS analysis is an essential tool to understand the charge transfer kinetics at the electrode/electrolyte interface as well as to discriminate between the resistive and capacitive mechanisms of the electrode materials. It provides the information about (i) the equivalent series resistance (R_{ESR}), which is the combination of contact resistance, intrinsic resistance of the material and the electrolyte solution and (ii) the charge transfer resistance (R_{ct}) at the solid/liquid interfaces [62]. The solution resistance (R_{ESR}) and charge transfer resistance (R_{ct}) of the electrode are calculated from the intercept at the x-axis of the semicircle at a higher frequency and high to the low-frequency region, respectively. The angle of the tail from the real axis (phase angle) at low frequency infers the dominant charge storage mechanisms. If the phase angle is equal to 45°, the system follows pseudocapacitive mechanism, and the phase angle approached to 90°, it reveals the capacitive charge storage mechanism. On the other hand, the phase angle is in between 45 and 90°, the system having both capacitive as well as a pseudocapacitive mechanism [63]. In the present study, the EIS spectra were recorded at open circuit potential and a different applied potential (bias potential) in a frequency range of 1 MHz–10 mHz and are shown in Fig. 6d and b (inset). The R_{ESR} and R_{ct} values for all the EIS curves are measured using an equivalent circuit (Fig. S8) through Z-fit software. It is found that the R_{ESR} (~2 Ohm) is almost same for all the applied potentials. However, the observed R_{ct} is changed with respect to the biased potentials like 0.5, 1.5, 42.8, 153.6, 290.3 and 576.6 Ohm, corresponding to −1.0, −0.8, −0.6, −0.4, −0.2, 0.0 V, respectively, which is due to the reduction in diffusion path length [64]. Similarly, the slope values, 60, 52, 28, 13, 0.5 and 0.3° are also changed with the applied potentials. On increasing the bias potential from low to high, the tail of the impedance curve (Warburg resistance) approaches towards 90°. Hence the higher phase angle of 60° at 0 V shows the pseudocapacitive as well as capacitive behavior, which reveals the charge storage mechanism of the material [65–67].

3.5. Asymmetric hybrid $CoSb_2O_4$||$Ni_3(Fe(CN)_6)_2(H_2O)$ supercapacitor

From the above electrochemical analysis of the prepared CB3 electrode, it is confirmed that the synthesized $CoSb_2O_4$ material could be used as a negative electrode material for supercapacitor application. Hence full cell is fabricated by using the CB3 as a negative electrode and the $Ni_3(Fe(CN)_6)_2(H_2O)$ as material as the positive electrode. Here 0.5 mg of CB3 is balanced by 1 mg of $Ni_3(Fe(CN)_6)_2(H_2O)$ electrode as per the mass balancing equation [42]. Further, the electrochemical performances of this fabricated hybrid supercapacitor are investigated through CV and GCD analysis and are shown in Fig. 7a–d. The electrochemical performances of both the individual CB3 and $Ni_3(Fe(CN)_6)_2(H_2O)$ electrodes at 2 mV s^{-1} are given in Fig. 7a. CV curves of both the electrodes show peaks and confirm the occurrence of redox mechanism in it. The CB3 electrode performs well up to −1.2 V without any gas evolution. Hence it is counterbalanced by $Ni_3(Fe(CN)_6)_2(H_2O)$ which shows redox reaction between 0 and 0.6 V. As a result; the assembled device is worked well up to the applied voltage of 0–1.6 V without any gas evolution and maintains the integrity of the device. Further, it is subjected to various scan rates such as 1, 2, 3, 4, 5, 10, 20, 30, 40 and 50 mV s^{-1} in Fig. 7b. The specific capacitance of 279, 183, 147, 130, 120, 97, 77, 66, 59 and 54 F g^{-1}, respectively, is obtained. Similarly, Fig. 7c shows the GCD curves at various current of 1, 2, 3, 4 and 5 mA and shows the capacitance of 30, 27, 23, 23 and 23 F g^{-1}, respectively. These results reveal the fact that specific capacitance is decreased while increasing scan rate. This is due to the fast electrode kinetics. Further Fig. 7d shows the specific capacitance *vs* cycle number plot. First 10 charge-discharge cycles are also given as an inset in Fig. 7d. For identifying the longevity of the device, GCD analysis is performed at 5 mA over 1000 cycles, and the capacitances are calculated. Initially, a decrease in capacitance is noticed for about 200 cycles, and then it becomes stable. This may be due to the lack of wettability of the electrode. After that, the

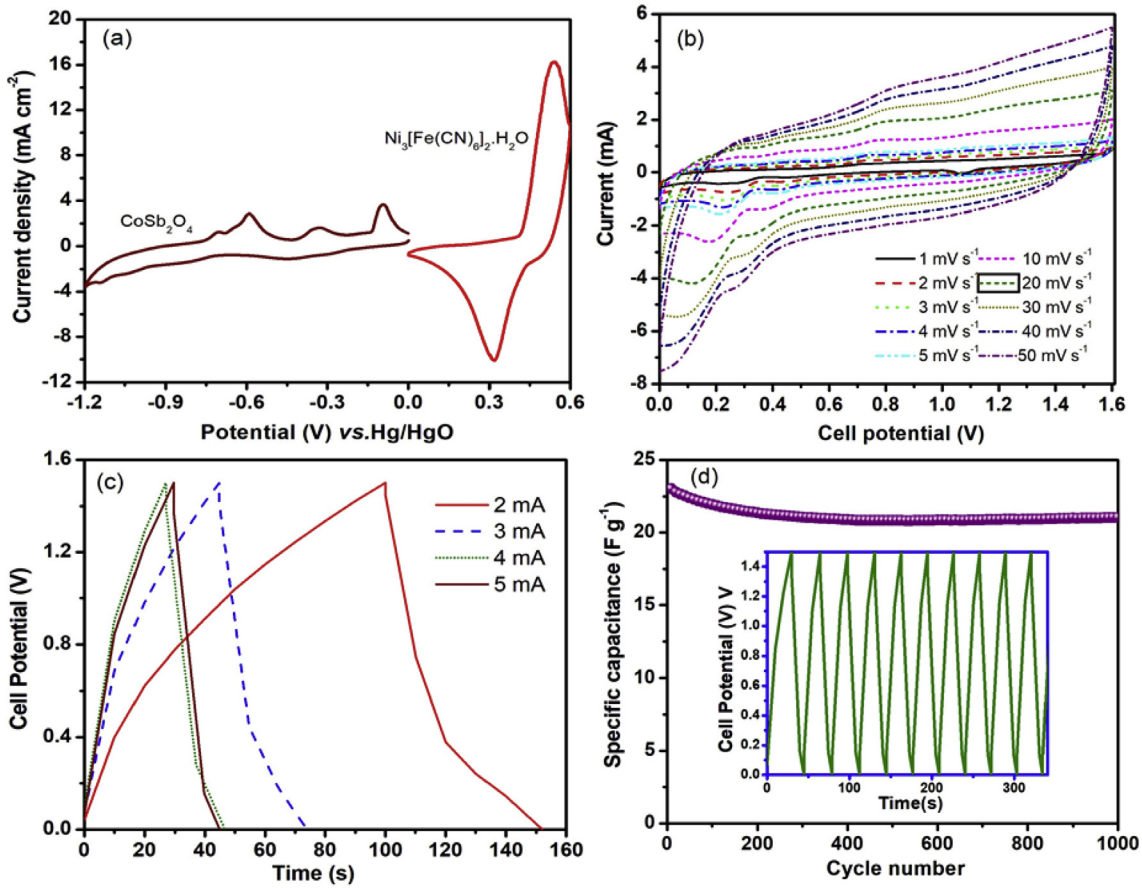

Fig. 7. (a) Comparative CV curves of CB3 and $Ni_3(Fe(CN)_6)_2(H_2O)$ at 2 mV s^{-1} in, (b) CV curves of ASC at various scan rates, (c) GCD curves of ASC at various current and (d) cycling stability of ASC at 5 mA over 1000 cycles (Inset) First 10 charge-discharge cycles.

excellent stability of almost 100% is obtained from the hybrid CB3||$Ni_3(Fe(CN)_6)_2(H_2O)$ supercapacitor. The Ragone plot of the fabricated asymmetric ($CoSb_2O_4$|| $Ni_3(Fe(CN)_6)_2(H_2O)$ supercapacitor is given in Fig. S9 in comparison with the reported Co based spinel compounds. The calculated maximum energy density is 8.3 Wh. Kg^{-1} and the power density is 2209 W kg^{-1}. The obtained values are higher than the previously reported Co based asymmetric supercapacitor including CoS||AC (5.3 Wh Kg^{-1} at 1800 W kg^{-1}) [68], and rGO||$CoMoO_4$ (8.17 Wh Kg^{-1} and 187.5 W kg^{-1}) [69]. Further, it is comparable with the $CoFe_2O_4$@C||AC (6.53 Wh Kg^{-1} at 0.72 kW kg^{-1} at 0.25 Ag^{-1}) [70] and $NiSb_2O_4$ ||Ni_3 $(Fe(CN)_6)_2(H_2O)$ (9.3 Wh Kg^{-1} at 405.3 kW kg^{-1}) [32]. Overall, this combined theoretical analysis of $CoSb_2O_4$ and the demonstrated electrochemical performance envisages the practical applications of the $CoSb_2O_4$ ||$Ni_3(Fe(CN)_6)_2(H_2O)$ asymmetric supercapacitor.

4. Conclusions

By varying the mole ratios of Co: Sb, $CoSb_2O_4$ were synthesized by hydrothermal method. At maximum 90 wt% of $CoSb_2O_4$ was confirmed by XRD and Rietveld refinement method and confirms the tetragonal crystal structure. The band gap value of 2.89 eV is obtained through the band structure calculations. Further, the valence state and functional groups such as Co–O and Sb–O were revealed through XPS and FTIR analysis. Moreover, the micrometre size particles were envisaged from FESEM and TEM analysis. The electrochemical analysis revealed the specific capacitance of 327 F g^{-1} at a current density of 1 mA at a negative potential window of 0 to −1.1 V. Further, device fabricated with $Ni_3(Fe(CN)_6)_2(H_2O)$ as positive electrode and offer the specific capacitance of 30 F g^{-1} at 1 mA and achieved a cycling stability of 100% over 1000 cycles. Hence the fabricated hybrid ($CoSb_2O_4$|| $Ni_3(Fe(CN)_6)_2(H_2O)$ could be used as a better energy storage device.

Acknowledgement

The author (A. Shanmugavani) would like to thank the CSIR, India for the award of Research Associateship (Ack no: 324494/2K15/1, File No: 09/472 (0176)/2016 – EMR-I, dated: 31/03/2017). Prof. Yun Sung Lee acknowledges the National Research Foundation of Korea (NRF) grant funded by the Korea government (Ministry of Science, ICT & Future Planning) (2016R1A4A1012224). Prof. L. Vasylechko acknowledges partial support of the Ukrainian Ministry of Education and Sciences under Project “Feryt”.

Appendix A. Supplementary data

Supplementary data related to this article can be found at https://doi.org/10.1016/j.electacta.2018.06.193.

References

[1] J. Chang, M. Jin, F. Yao, T.H. Kim, V.T. Le, H. Yue, F. Gunes, B. Li, A. Ghosh, S. Xie, Asymmetric supercapacitors based on graphene/MnO_2 nanospheres and graphene/MoO_3 nanosheets with high energy density, Adv. Funct. Mater. 23 (2009) 5074.
[2] W. Zuo, R. Li, C. Zhou, Y. Li, J. Xia, J. Liu, Battery-supercapacitor hybrid devices:

recent progress and future prospects, Adv. Sci. 4 (2017), 160053.
[3] G. Xiong, P. He, B. Huang, T. Chen, Z. Bo, T.S. Fisher, Graphene nanopetal wire supercapacitors with high energy density and thermal durability, Nano Energy 38 (2017) 127.
[4] M. Aghazadeh, A. Rashidi, M. Reza Ganjali, M.G. Maragheh, Nickel oxide nanorods/plates as a high performance electrode materials for supercapacitors; electrosynthesis and evolution of charge storage ability, Int. J. Electrochem. Sci. 11 (2016) 11002.
[5] M. Aghazadeh, I. Karimzadeh, M. Reza Ganjali, Preparation of nano-sized bismuth-doped Fe_3O_4 as an excellent magnetic material for supercapacitor electrodes, J. Electron. Mater. 47 (2018) 3026.
[6] X.-H. Xia, J.—P. Tu, X.—L. Wang, C.—D. Gu, X.—B. Zhao, Mesoporous Co_3O_4 monolayer hollow-sphere array as electrochemical pseudocapacitor material 47 (2011) 5786.
[7] M. Aghazadeh, M.G. Maragheh, M.R. Ganjali, P. Norouzi, D. Gharailou, F. Faridbod, Electrochemical preparation and supercapacitive performance of a-MnO_2 nanospheres with secondary wall-like structures, J. Mater. Sci. Mater. Electron. 27 (2016) 7707.
[8] M. Aghazadeh, M. Asadi, M.R. Ganjali, P. Norouzi, B. Sabour, M. Emamalizadeh, Template-free preparation of vertically-aligned Mn_3O_4 nanorods as high supercapacitive performance electrode material, Thin Solid Films 634 (2017) 24.
[9] H. Wang, H.S. Catalogue, Y. Liang, H. Dai, Ni$(OH)_2$ nanoplates grown on graphene as advanced electrochemical pseudocapacitor materials, J. Am. Chem. Soc. 132 (2010) 7477.
[10] T. Liu, L. Finn, M. Yu, H. Wang, T. Zhai, X. Lu, Y. Tong, Y. Li, Polyaniline and polypyrrole pseudocapacitor electrodes with excellent cycling stability, Nano Lett. 14 (2014) 2522.
[11] Y. Zhang, C. Sun, H. Su, W. Huang, X. Dong, N-doped carbon coated hollow $Ni_xCo_{9-x}S_8$ urchins for a high performance supercapacitor, Nanoscale 7 (2015) 3155.
[12] J.R. Gavarri, A.W. Hewat, Les antimonides antiferromagnetiques $MnSb_2O_4$ et $NiSb_2O_4$, J. Solid State Chem. 49 (1983) 14.
[13] R. Alcantra, F.J. Fernandez-madrigal, P. Lavela, J.L. Triado, J.C. Jumas, J. Oliver-Fourcade, Electrochemical reaction of lithium with the $CoSb_3$ skutterudite, J. Mater. Chem. 9 (1999) 2417.
[14] L.J. Jhang, X.B. Zhao, X.B. Jiang, C.P. Lv, G.S. Cao, Study on the insertion behaviors of Lithium-ions into $CoFe_3Sb_{12}$ based electrodes, J. Power Sources. 94 (2001) 92.
[15] D. Larcher, A.S. Prakash, L. Laffont, M. Womes, J.C. Jumas, J. Oliver Fourcade, M.S. Hedge, J.M. Tarascon, Reactivity of antimony oxides and MSb_2O_6 (M = Cu , Ni , Co), tirutile-type phases with metallic lithium, J. Electrochem. Soc. 153 (2006) A1778.
[16] B.P. De Laune, C. Greaves, Structural and magnetic characterisation of $CoSb_2O_4$, and the substitution of Pb2+ for Sb3+, J. Solid State Chem. 187 (2012) 225.
[17] K. Jibin, M.V. Reddy, G.V. Subba Rao, U.V. Varadaraju, Pb_3O_4 type antimony oxides MSb_2O_4 (M = Co, Ni) as anode for Li-ion batteries, Electrochim. Acta 71 (2012) 227.
[18] G. Kresse, D. Joubert, From ultrasoft pseudopotentials to the projector augmented-wave method, Phys. Rev. B 59 (1999) 1758.
[19] J.P. Perdew, K. Burke, M. Ernzerhof, Generalized gradient approximation made simple, Phys. Rev. Lett. 77 (1996) 3865.
[20] S.L. Dudarev, G.A. Botton, S.Y. Savrasov, C.J. Humphreys, A.P. Sutton, Electron-energy-loss spectra and the structural stability of nickel oxide: an LSDA+U study, Phys. Rev. B Condens. Matter 57 (1998) 1505.
[21] M. Lalitha, N. Yuvarani, L. Senthilkumar, Calcium decorated and doped phosphorene for gas adsorption, Appl. Surf. Sci. 377 (2016) 311.
[22] M. Lalitha, L. Senthilkumar, S.K. Bhatia, Influence of in-plane Stone—Thrower—Wales defects and edge functionalisation on the adsorption of CO_2 and H_2O on graphene, RSC Adv. 4 (2014) 39576.
[23] A. Shanmugavani, R. Kalai Selvan, Improved electrochemical performances of $CuCo_2O_4$/CuO nanocomposites for asymmetric supercapacitors, Electrochim. Acta 188 (2016) 852.
[24] R. Kalai Selvan, C.O. Augustin, J.L. Berchmans, R. Saraswathi, Combustion synthesis of $CuFe_2O_4$, Mater. Res. Bull. 38 (2003) 41.
[25] A. Shanmugavani, R. Kalai Selvan, Microwave assisted reflux synthesis of $NiCo_2O_4$/NiO composite: fabrication of high performance asymmetric supercapacitor with Fe_2O_3, Electrochim. Acta 189 (2016) 283.
[26] L. Akselrud, Y. Grin, WinCSD: software package for crystallographic calculations (Version 4), J. Appl. Crystallogr. 47 (2014) 803.
[27] P.M. De-Wolff, The crystal structure of $Co_2(OH)_3Cl$, Acta Crystallogr. 6 (1953) 359.
[28] G. Westin, M. Nygren, On the formation of M2+-Sb3+-alkoxide precursors and sol-gel processing of M-S b oxides with M =Cr, Mn, Fe, Co, Ni, Cu and Zn, J. Mater. Sci. 27 (1992) 1617.
[29] J.R. Gavarri, Evolution structurale d'oxydes isomorphes MeX_2O_4: relation entre dilatation, vibrations et rigidite, J. Solid State Chem. 43 (1982) 12.
[30] J.R. Gavarri, R. Chater, J. Ziolkowski, The chemical bonds in $MeSb_2O_4$ (Me = Mn, Ni, Fe, Zn) isomorphous compounds: thermal expansion, force constants, energies, J. Solid State Chem. 73 (1988) 305.
[31] Hk Müller-Buschbaum, The crystal chemistry of AM_2O_4 oxometallates, J. Alloys Compd. 349 (2003) 49.
[32] A. Shanmugavani, M. Lalitha, S. Yuvaraj, L. Vasylechko, D. Meyrick, L. Senthilkumar, R. Kalai Selvan, Facile hydrothermal synthesis and first principle computational studies of $NiSb_2O_4$ and its electrochemical properties with $Ni_3(Fe(CN)_6)_2(H_2O)$ for hybrid supercapacitors, Chem. Select 2 (2017) 6823.
[33] H.C. Chen, J.J. Jiang, L. Zhang, H.Z. Wan, T. Qi, D.D. Xia, Highly conductive $NiCo_2S_4$ urchin-like nanostructures for high-rate pseudocapacitors, Nanoscale 5 (2013) 8879.
[34] A. Hoffmann da Rocha, E. Bueno Pires, A.D. Silveira Nectoux, S.L. Pereira Dias, É.C. Lima, L.T. Radtke Kubota, Preparation and electrochemical behavior of the CA/TiO_2/Sb_2O_5 composite electrode modified with p-benzoquinone, J. Electroanal. Chem. 690 (2013) 74.
[35] J.F. Marco, J.R. Gancedo, M. Gracia, J.L. Gautier, E. Rıos, F.J. Berry, Characterization of the nickel cobaltite, $NiCo_2O_4$, prepared by several methods: an XRD, XANES, EXAFS, and XPS study, J. Solid State Chem. 153 (2000) 74.
[36] Y.E. Roginskaya, O.V. Morozova, N. ELubnin, Y.E. Ulitina, G.V. Lopukhova, S. Trasatti, Characterization of bulk and surface composition of $Co_xNi_{1-x}O_y$ mixed oxides for electrocatalysis, Langmuir 13 (1997) 4621.
[37] F. Rosi, V. Manuali, C. Miliani, B.G. Brunetti, A. Sgamellotti, T. Grygar, D. Hradil, Raman scattering features of lead pyroantimonate compounds. Part I: XRD and Raman characterization of $Pb_2Sb_2O_7$ doped with tin and zinc, J. Raman Spectrosc. 40 (2009) 107.
[38] H.Y. Guan, C.L. Shao, S.B. Wen, B. Chen, J. Gong, X.H. Yang, A novel method for preparing Co_3O_4 nanofibers by using electrospun PVA/cobalt acetate composite fibers as precursor, Mater. Chem. Phys. 82 (2003) 1002.
[39] S. Vijayakumar, S. Nagamuthu, G. Muralidharan, Supercapacitor studies on NiO nanoflakes synthesized through a microwave route, ACS Appl. Mater. Interfaces 5 (2013) 2188.
[40] R. Ding, L. Qi, M. Jia, H. Wang, Facile and large-scale chemical synthesis of highly porous secondary submicron/micron-sized $NiCo_2O_4$ materials for high-performance aqueous hybrid AC-$NiCo_2O_4$ electrochemical capacitors, Electrochim. Acta 107 (2013) 494.
[41] V.S. Kumbhar, A.D. Jagadale, N.M. Shinde, C.D. Lokhande, Chemical synthesis of spinel cobalt ferrite ($CoFe_2O_4$) nano-flakes for supercapacitor application, Appl. Surf. Sci. 259 (2012) 39.
[42] K. Vijaya Sankar, R. Kalai Selvan, Fabrication of flexible fiber supercapacitor using covalently grafted $CoFe_2O_4$/reduced graphene oxide/polyaniline and its electrochemical performances, Electrochim. Acta 213 (2016) 469.
[43] X. Xia, Q. Hao, W. Wang, X. Wang, One-step synthesis of $CoMoO_4$/graphene composites with enhanced electrochemical properties for supercapacitors, Electrochim. Acta 99 (2013) 253.
[44] Nm V. Kannan, A.I. Inamdar, S.M. Pawar, H.-S. Kim, H.-C. Park, H. Kim, H. Im, Y. Sik Chae, Facile route to NiO nanostructured electrode grown by oblique angle deposition technique for supercapacitors, ACS Appl. Mater. Interfaces 8 (2016) 17220.
[45] C.L.M. Charles, S. Jung, C.P. Jonas, F.J. Thomas, Benchmarking heterogeneous electrocatalysts for the oxygen evolution reaction, J. Am. Chem. Soc. 135 (2013) 16977.
[46] B. You, Y. Sun, Hierarchically porous nickel sulfide multifunctional superstructures, Adv. Energy Mater. 6 (2016) 1502333.
[47] R. Yue, F. Ren, C. Wang, J. Xu, Y. Du, Facile preparation of flower-like graphene nanosheet clusters with the assistance of copper particles and their application in supercapacitors, RSC Adv. 4 (2014) 500.
[48] J. Huang, Y. Li, Y. Xia, J. Zhu, Q. Yi, H. Wang, J. Xiong, Y. Sun, G. Zou, Flexible cobalt phosphide network electrocatalyst for hydrogen evolution at all pH values, Nano Res. 10 (2017) 1010.
[49] Atlas of Eh-pH Diagrams, Intercomparison of Thermodynamic Databases, Geological Survey of Japan Open File Report No.419, 2005.
[50] A. El-R. El-Sayed, A.M. Shaker, H.G. El-Kareem, Anodic behaviour of antimony and antimony-tin alloys in alkaline solutions, Bull. Chem. Soc. Jpn. 76 (2003) 1527—1535.
[51] F. Quentel, M. Filella, C. Elleouet, C.L. Madec, Kinetic studies on Sb(III) oxidation by hydrogen peroxide in aqueous solution, Environ. Sci. Technol. 38 (2004) 2843.
[52] X. Guo, X. Xie, S. Choi, Y. Zhao, H. Liu, C. Wang, S. Chang, G. Wang, Sb_2O_3/MXene(Ti_3C_2Tx) hybrid anode materials with enhanced performance for sodium-ion batteries, J. Mater. Chem. A (2017) 12445.
[53] K. Sik Hong, D.-H. Nam, S.-J. Lim, D. Sohn, T.-H. Kim, H. Kwon, Electrochemically synthesized Sb/Sb_2O_3 composites as high-capacity anode materials utilizing a reversible conversion reaction for Na-ion batteries, ACS Appl. Mater. Interfaces 12 (2015) 17264.
[54] K. Li, H. Liu, G. Wang, Sb_2O_3 nanowires as anode material for sodium-ion battery, Arabian J. Sci. Eng. 39 (2014) 6589.
[55] D. Li, D. Yan, J. Ma, W. Qin, X. Zhang, T. Lu, L. Pan, One-step microwave-assisted synthesis of Sb_2O_3/reduced graphene oxide composites as advanced anode materials for sodium-ion batteries, Ceram. Int. 42 (2016) 15634.
[56] D.-H. Nam, K.-S. Hong, S.J. Lim, M.-J. Kim, H.-S. Kwon, High-performance Sb/Sb_2O_3 anode materials using a polypyrrole nanowire network for Na-Ion batteries, Small 11 (2015) 2885.
[57] S.D. Perera, X. Ding, A. Bhargava, R. Hovden, A. Nelson, L.F. Kourkoutis, R.D. Robinson, Enhanced supercapacitor performance for equal Co—Mn stoichiometry in colloidal $Co_{3-x}Mn_xO_4$ nanoparticles, in additive-free electrodes, Chem. Mater. 27 (2015) 7861.
[58] B. Kim, C. Justin Raj, W. Cho, W. Lee, H. Jeong, K. Hyun Yu, Enhanced electrochemical properties of cobalt doped manganese dioxide nanowires, J. Alloys Compd. 617 (2014) 491.
[59] L. Ren, J. Chen, X. Wang, M. Zhi, J. Wu, X. Zhang, Facile synthesis of flower-like

$CoMn_2O_4$ microspheres for electrochemical supercapacitors, RSC Adv. 5 (2015) 30963.
[60] Y. Zhao, F. Teng, Z. Liu, Q. Du, J. Xu, Y. Teng, Electrochemical performances of asymmetric super capacitor fabricated by one-dimensional $CoMoO_4$ nanostructure, Chem. Phys. Lett. 664 (2016) 23.
[61] W. Li, X. Wang, Y. Hu, L. Sun, C. Gao, C. Zhang, H. Liu, M. Duan, Hydrothermal synthesized of $CoMoO_4$ microspheres as excellent electrode material for supercapacitor, Nanoscale Res. Lett. 13 (2018) 120.
[62] W. Sun, X. Chen, Preparation and characterization of polypyrrole films for three-dimensional micro supercapacitor, J. Power Sources 193 (2009) 924.
[63] H.M. Shiri, A. Ehsani, A novel and facile route for the electrosynthesis of Ho_2O_3 nanoparticles and its nanocomposite with p-type conductive polymer:characterisation and electrochemical performance, Bull. Chem. Soc. Jpn. 89 (2016) 1201.
[64] M. Naseri, L. Fotouhi, A. Ehsani, Facile electrosynthesis of nano flower like metal-organic framework and its nanocomposite with conjugated polymer as a novel and hybrid electrode material for highly capacitive pseudocapacitors, J. Colloid Interface Sci. 484 (2016) 314.
[65] J. Torabian, M.G. Mahjani, H. Mohammad Shiri, A. Ehsani, J. Shabani Shayeh, Facile electrosynthesis, characterisation and electrochemical performance of poly ortho aminophenol/$Al_5Y_3O_{12}$ nanocomposite as a new high efficient supercapacitor, RSC Adv. 6 (2016) 41045.
[66] W. Sugimoto, H. Iwata, K. Yokoshima, Y. Murakami, Y. Takasu, Proton and electron conductivity in hydrous ruthenium oxides evaluated by electrochemical impedance spectroscopy: the origin of large capacitance, J. Phys. Chem. B 109 (2005) 7330.
[67] H. Farsi, F. Gobal, H. Raissi, S. Moghiminia, On the pseudocapacitive behavior of nanostructured molybdenum oxide, J. Solid State Electrochem. 14 (2010) 643.
[68] K. Subramani, N. Sudhan, R. Divya, M. Sathish, All-solid-state asymmetric supercapacitors based on cobalt hexacyanoferrate-derived CoS and activated carbon, RSC Adv. 7 (2017) 6648.
[69] G.K. Veerasubramani, K. Krishnamoorthy, S.J. Kim, Electrochemical performance of an asymmetric supercapacitor based on graphene and cobalt molybdate electrodes, RSC Adv. 5 (2015) 16319.
[70] Y. Zhao, Y. Xu, J. Zeng, B. Kong, X. Geng, D. Li, X. Gao, K. Liang, L. Xu, J. Lian, S.H. Huang, J. Qiu, Y. Huang, H. Li, Low-crystalline mesoporous $CoFe_2O_4$/C composite with oxygen vacancies for high energy density asymmetric supercapacitors, RSC Adv. 7 (2017) 55513.